


Limbostomy: Longitudinal Intravital Microendoscopy in Murine Osteotomies

Jonathan Stefanowski,^{1,2†}  Alexander F. Fiedler,^{2,5†}  Markus Köhler,^{2,5} Robert Günther,² Wjatscheslaw Liublin,² Martin Tschaikner,² Ariana Rauch,² David Reismann,² Romano Matthys,⁶ Reto Nützi,⁶ Maria Gabriele Bixel,⁷  Ralf H. Adams,⁷ Raluca A. Niesner,^{2,5} Georg N. Duda,^{3,4‡} Anja E. Hauser^{1,2‡*} 

¹Department of Rheumatology and Clinical Immunology, Charité – Universitätsmedizin Berlin, Corporate Member of Freie Universität Berlin, Humboldt-Universität zu Berlin, and Berlin Institute of Health, Berlin, Germany

²Deutsches Rheuma-Forschungszentrum (DRFZ) Berlin, a Leibniz Institute, Berlin, Germany

³Charité – Universitätsmedizin Berlin, Corporate Member of Freie Universität Berlin, Humboldt-Universität zu Berlin, and Berlin Institute of Health, Berlin Institute of Health Center for Regenerative Therapies, Berlin, Germany

⁴Charité – Universitätsmedizin Berlin, Corporate Member of Freie Universität Berlin, Humboldt-Universität zu Berlin, and Berlin Institute of Health, Julius Wolff Institute, Berlin, Germany

⁵Freie Universität Berlin, Veterinary Medicine, Dynamic and Functional *in vivo* Imaging, Berlin, Germany

⁶RISystem AG, Landquart, Switzerland

⁷Max Planck Institute for Molecular Biomedicine, Münster, Germany

Received 23 October 2019; Revised 20 January 2020; Accepted 24 February 2020

Grant sponsor: Deutsche Forschungsgemeinschaft, Grant numbers: DFG FOR 2165/HA5354/6-2, DFG TRR130 TP C01, SPP1937/HA5354/8-2

Additional Supporting Information may be found in the online version of this article.

• Abstract

Bone healing involves the interplay of immune cells, mesenchymal cells, and vasculature over the time course of regeneration. Approaches to quantify the spatiotemporal aspects of bone healing at cellular resolution during long bone healing do not yet exist. Here, a novel technique termed Limbostomy is presented, which combines intravital microendoscopy with an osteotomy. This design allows a modular combination of an internal fixator plate with a gradient refractive index (GRIN) lens at various depths in the bone marrow and can be combined with a surgical osteotomy procedure. The field of view (FOV) covers a significant area of the fracture gap and allows monitoring cellular processes *in vivo*. The GRIN lens causes intrinsic optical aberrations which have to be corrected. The optical system was characterized and a postprocessing algorithm was developed. It corrects for wave front aberration-induced image plane deformation and for background and noise signals, enabling us to observe subcellular processes. Exemplarily, we quantitatively and qualitatively analyze angiogenesis in bone regeneration. We make use of a transgenic reporter mouse strain with nucleargreen fluorescent protein and membrane-bound tdTomato under the Cadherin-5 promoter. We observe two phases of vascularization. First, rapid vessel sprouting pervades the FOV within 3–4 days after osteotomy. Second, the vessel network continues to be dynamically remodeled until the end of our observation time, 14 days after surgery. Limbostomy opens a unique set of opportunities and allows further insight on spatiotemporal aspects of bone marrow biology, for example, hematopoiesis, analysis of cellular niches, immunological memory, and vascularization in the bone marrow during health and disease. © 2020 The Authors. *Cytometry Part A* published by Wiley Periodicals, Inc. on behalf of International Society for Advancement of Cytometry.

• Key terms

intravital microscopy; bone regeneration; osteotomy; bone vascularization; internal fixation; chronic window; multiphoton microscopy; GRIN lens; wave front correction; aberration correction; bone microendoscopy

REGENERATIVE healing of tissues is a highly dynamic process that shows a very distinct spatial distribution of the cells involved, governing self-organization of the forming tissue. Bone healing can serve as a model system for such dynamic healing cascades, specifically since bone has the unique capability of complete restoration without scar formation. To understand the underlying principles of this early self-assembly in healing, however, a better insight into the *in vivo* dynamics of these cellular processes is needed. From *ex vivo* and histological observations, we have learned that fracture healing is a tightly regulated process, which occurs in overlapping but distinct phases and involves the interplay of multiple cell compartments, such as the immune system, the vasculature, and various mesenchymal cells. Directly

*Correspondence to: Anja E. Hauser, Charité – Universitätsmedizin Berlin, Corporate Member of Freie Universität Berlin, Humboldt-Universität zu Berlin, and Berlin Institute of Health, Department of Rheumatology and Clinical Immunology, Berlin, Germany
Email: hauser@drfz.de; anja.hauser-hankeln@charite.de

[†]These authors contributed equally to this study.

[‡]These authors contributed equally to this study.

Published online 20 March 2020 in Wiley Online Library
(wileyonlinelibrary.com)

DOI: 10.1002/cyto.a.23997

© 2020 The Authors. *Cytometry Part A* published by Wiley Periodicals, Inc. on behalf of International Society for Advancement of Cytometry.

This is an open access article under the terms of the Creative Commons Attribution-NonCommercial License, which permits use, distribution and reproduction in any medium, provided the original work is properly cited and is not used for commercial purposes.

after injury, a fracture hematoma forms, accompanied by the release of inflammatory mediators and the recruitment of immune cells. The initial, pro-inflammatory phase transits into an anti-inflammatory phase and as inflammation wanes, soft callus is formed, comprising fibro-cartilaginous tissue, which subsequently becomes mineralized and is therefore termed hard callus. Finally, in the remodeling phase, this newly formed bone is refined in an orchestrated interplay between cells of hematopoietic and mesenchymal origin (including osteoblasts and osteoclasts), which remodel the tissue, until an intact and fully functional bone structure is restored (1–3).

However, certain risk factors like age (4,5) or metabolic disorders (6) can delay or even impede the healing process significantly, reflected in fracture healing disorders which occur in 5–10% of patients (7). In order to further define risk factors and design patient-oriented therapeutic strategies, a detailed understanding of the processes underlying bone regeneration is necessary.

It has become evident that these regenerative cascades involve a dynamic and at least partly directed interaction between single cells of various compartments. However, mainly due to a lack of appropriate tools and technology, the details of this interplay, especially its spatiotemporal aspects, are not fully understood. Histological analyses, which demonstrated a role for the innate (8–10) and adaptive (4,11) arms of the immune system, have been performed. These analyses represent *ex vivo* snapshots of the tissue state taken from individuals at defined time points and have laid the foundation for a comprehensive analysis of the cellular composition at the injury site at various phases of bone regeneration. However, they did not allow conclusions on the dynamic regulation of cellular interaction events and interplay of cells with the surrounding matrix over time and in space. Examples for such events and interplays are endothelial cells sprouting into a site of injury, the recruitment of immune cells to an injury, the dynamic transition from the pro- to the anti-inflammatory phase, the dynamics within the mesenchymal compartment promoting callus formation, and finally, the processes of bone remodeling.

Two-photon intravital imaging of the bone marrow has become an important tool for the characterization and quantification of cellular dynamics in immunology (12). Intravital imaging has significantly contributed to our understanding of the dynamic nature of hematopoiesis (13–16) as well as the

dynamics of mature immune cells in the bone marrow (17,18) and their interactions with mesenchymal compartments (19). In many reports, marrow islands within the calvarial flat bone are visualized through the thin bone layer on the top of the skull (3,14,16,18,20–25). There are also reports of intravital multiphoton imaging being performed in long bones, such as the metatarsal bones in young animals (26) and the explanted femur (27). The femur bone marrow has also been analyzed using an external window (28). Imaging in the tibia has been performed using an approach in which an acute injury is introduced to the skin and the bone surface, in order to achieve thinning of the cortex (15,17,19). A similar approach in the tibia has been used for longitudinal imaging (21). In order to optically access the bone marrow, the cortical layer is thinned to 30–50 μm (15,17,19). Finally, access to the bone marrow has been achieved by generating subcutaneous ossicles from medical-grade polycaprolactone-calcium phosphate (mPCL-CaP) scaffolds and application of bone morphogenetic protein (BMP)-7, embedded in fibrin glue (29).

While all these approaches allowed conclusions on cellular dynamics in the tissue, observation time is limited to relatively short time periods, typically in the scale of hours. Chen et al. reported the insertion of a femoral window, which enables observation over the course of 10 days (28). However, none of these procedures covers the time and tissue location necessary to observe the process of endochondral bone regeneration in one and the same individual.

We have recently developed a microendoscopic implant, which allows us to image in the bone marrow of a femoral mouse bone, at the same tissue location, over the course of several months (30,31). The system is based on a gradient refractive index (GRIN) lens attached to an internal bone fixator (MouseFix system) (32), which results in stable fixation of the optical system in the femur, suitable for two-photon microscopy. Implantation of the microendoscopic lens requires opening the cortex with a drill, so the whole procedure closely resembles the damage induced by drill hole injury models. In fact, it can be used to monitor tissue regeneration after this type of injury. Thus, we have previously been able to demonstrate the changes in tissue composition following a drill hole injury, in particular the high degree of vascular dynamics occurring during the regeneration phase.

While drill hole injuries constitute important tools for studying bone regeneration, they mainly represent a form of

regeneration termed intramembranous ossification, where bone is formed directly from mesenchymal progenitors (33). This does not fully recapitulate all the phases of regeneration, which occur during endochondral ossification following a fracture, where a cartilaginous intermediate is generated, which then becomes mineralized and remodeled. In order to fully understand the orchestrated processes occurring during endochondral bone regeneration at a cellular and tissue level, it is highly desirable to combine longitudinal intravital two-photon imaging in bone (LIMB) with an osteotomy model.

In addition, flat bones and long bones display similarities and differences in cell distribution (34,35), ontogeny, and protein composition (36). It is known that the lack of mechanical load leads to a reduction of matrix protein expression (37,38) and bone regeneration of comparable defects is faster in long bones compared to calvarial flat bone (39). An intravital imaging approach for bone regeneration in long bones will help understanding those functional differences between injury regeneration at different sites, and improve our understanding of this process at tissue sites of high relevance in terms of translation. Here, we present a novel technology for intravital imaging termed Limbostomy, which allows to perform longitudinal intravital imaging directly in osteotomized areas, and to analyze spatiotemporal aspects at a cellular level directly at the site of endochondral bone regeneration, in a field of view (FOV) covering a substantial area of the fracture gap.

The microendoscopic lenses used for this approach show inherent optical aberrations, which cause positional or amplitude discrepancies of the light wave fronts at the focal plane, leading to artifacts during image acquisition. These include chromatic aberration and spherical wave front aberrations, and result in lower FOV due to less contrast and sharpness in outer radial areas and reduced spatial resolution (40).

In order to gather reliable spatial information using our technique, we thoroughly characterized the wave front and chromatic aberrations and designed a postprocessing pipeline to correct the imaging results in Limbostomy. In this way, we access a cylindrical volume of 400 μm in diameter and up to a theoretical 200 μm depth at high imaging quality, resulting in a promising tool for applications across multiple disciplines.

MATERIAL AND METHODS

Mice

All animal experiments were approved by the local animal protection authority (LaGeSo Berlin; permission number G0302/17) following the German Animal Welfare Act. Cdh5-GFP-tdT mice express a membrane-tagged tandem tomato fluorescent protein (tdT) and histone 2B linked enhanced green fluorescent protein (GFP) under a transgenic VE-cadherin (Cdh5) promoter (41). Animals were bred in our colony and kept in a conventional specific pathogen-free barrier facility. Prior to surgery, 14-week-old female animals received Buprenorphine (0.03 mg/kg; Temgesic[®], Indivior Deutschland GmbH, Mannheim, Germany) s.c. as analgesic, one injection of 0.04% Enrofloxacin (Baytril[®], 10 mg/kg body weight Bayer AG, Leverkusen, Germany) (42), and

dexpanthenol-containing eye ointment (Bepanthen[®], Bayer AG, Leverkusen, Germany). Pain was inhibited using Tramadol (0.05 mg/ml; Grünenthal, Aachen, Germany) for 3 days after surgery in drinking water ad libitum. For calculation of the gap size, results from other female mice of the same genetic background (C57BL/6) have been included.

Lens Gluing Process

In order to fix the lens in the endoscope, tubing glue was applied. The process was recorded and can be observed in the Supporting Information Movie S1. The tubing was positioned with one hole downward onto an inverted stripe of tape, which sealed the hole and simultaneously held the tubing in position. The lens was inserted into the tubing and two drops of two-component glue (EPO-TEK 301-2, John P. Kummer GmbH, Augsburg, Germany) were transferred into the exposed hole using a syringe needle. The glue was cured at 65°C overnight.

Limbostomy Imaging Procedure

For intravital imaging, anesthesia was induced with 2.0% and maintained with 1.25–1.5% of isoflurane. Mice were positioned on a heating pad at 38°C and dexpanthenol ointment was applied on both eyes to protect them from drying out. Under anesthesia, the set screw was removed, the lens examined for particles, and, if necessary, wiped clean with a dry spear swab. The reference plate was slid into a plastic adapter and secured into the stage at a fixed vertical rotation angle. The stage, including the mouse, was positioned onto the intravital microscope table (LaVision BioTec GmbH, Bielefeld, Germany) under an upright laser-scanning microscope based on a commercial scan head (TriMScope II, LaVision BioTec GmbH, Bielefeld, Germany). Using a 20 \times objective lens (IR-coating, NA 0.45, Olympus, Hamburg, Germany), the imaging plane was focused on the GRIN lens outer surface (length ca. 5.07 mm, diameter = 0.60 mm; NEM-060-10-10-850-S-1.0p, GRINTECH GmbH, Jena, Germany). Using the InspectorPro software (version 208, LaVision BioTec GmbH, Bielefeld, Germany), the focal plane was elevated 200 μm . From there, the focus was gradually moved downward (approximately 50 μm) at low laser power (wavelength = 980 nm; Ti-Sapph Laser, Coherent, Dieburg, Germany) until the surface of the GRIN lens inside the tissue was visible. Fluorophores (tdT, GFP) and Qtracker 655 Vascular Labels (Qtracker655, Q21021MP, Thermo Fisher, Waltham, MA, USA) were excited at 980 nm. 3D time-lapse stacks were acquired with a FOV of 505 \times 505 px (500 \times 500 μm , frequency = 1000, line average = 4, unidirectional) using linear power adaption at a z-step size of 5 μm and up to 19 z-steps at a time interval of 1 min over a total duration of up to 2 h. Qtracker 655 were injected into the tail vein prior to acquisition (2–3 μl per animal). Emitted light was detected with photomultiplier tubes in the ranges of 466 \pm 20, 525 \pm 25, 593 \pm 20, and 655 \pm 20 nm. GFP was detected at 525 \pm 25 nm, tdT at 593 \pm 20 nm, Qtracker 655 at 655 \pm 20 nm, and second harmonic generation second harmonic generation (SHG) signal at 593 \pm 20 nm. After

imaging, the mouse was removed from the stage and the lens was secured using a set screw.

Image Correction

The background was corrected with a white top-hat morphological filter (based on the empirically determined size and shape of the cells) of the MorphoLibJ Plugin in FIJI. This filter homogenizes the uneven background and fluorescence signal intensities in the edge and central FOV regions, through performing a mathematical morphological opening (dilation) of the image (43). Finally, in order to reduce noise, a despeckling algorithm was applied to the images using the despeckle function in FIJI.

Image Analysis

Stack images were loaded with Imaris Software (v9.3.0, Bitplane, Zurich, Switzerland) and signal intensity was corrected over time using the *normalize time points* function. A *reference frame* was placed at the center of the image. Next, surfaces for nuclei were reconstructed based on the GFP signal and the vessels based on the tdTomato signal. Nuclei were filtered by *track displacement* (10 μm) and *track duration* (496 s) for moving nuclei. Based on the *reference frame*, the statistics *track position mean*, *track position start*, *track displacement*, and *track velocity* were exported for moving cells. *Volume* was exported for unfiltered vessel and nuclei surfaces. *Track velocity* is the length of the track path divided by the duration of the track.

Analysis toward the center of the FOV

In order to determine the direction of the moving cells, the length of the vectors in the *reference frame* “center” was calculated for *track position start* (defined by the value of the X, Y track start positions; $\left| \vec{a} \right|$) and *track position mean* (defined by the mean value of X, Y track coordinates positions; $\left| \vec{b} \right|$) in X, Y. The *difference of vector lengths from center* $\left| \vec{a} \right| - \left| \vec{b} \right|$ was calculated and normalized to the *track displacement* (or: *displacement*; the object’s track displacement is the distance between the first and last object’s position along the selected-axis) in order to account for the actual distance between start and end position. Positive values indicate a movement toward the center, negative values away from the center.

Analysis of the surface volumes

Imaging volume was based on the theoretical volume of the stack. *Total nuclei volume* was the sum of all nuclei surfaces averaged over time. *Total vessel volume* was the sum of all vessel surfaces averaged over time.

Histology

Femoral bones were explanted, muscles largely removed so that osteotomized bone parts maintained one entity. Tissue was fixed using 4% electron microscopy-grade paraformaldehyde in phosphate-buffered saline (PBS) for 4 h at 4°C, washed in PBS, and run through a sucrose gradient (10%,

20%, 30%; for 12–24 h). Bones were frozen in SCEM medium (Sectionlab, Hiroshima, Japan), cut into slices of 7 μm using Kawamoto’s film method (44), and stored at -80°C . For immunofluorescence, individual sections were thawed, rehydrated in PBS, blocked with 10% donkey serum, and stained with antibodies in PBS/0.1% Tween 20/5% donkey serum containing 4',6-diamidino-2-phenylindole (DAPI) for 1–2 h. Target proteins were identified using antibodies against Emcn (V.7C7 unconjugated, sc-65495, 1:100, Santa Cruz Biotechnology, Inc, Dallas, TX, USA). Primary antibodies were stained with secondary antibodies (1:500, anti-rat conjugated AF594, A21209, Thermo Fisher, Waltham, MA, USA). Samples were washed between steps and after staining with PBS/0.1% Tween 20 for 3×5 min. Stained samples were kept in PBS for 5 min, embedded using aqueous mounting medium (Fluoromount, Thermo Fisher, Waltham, MA, USA), and analyzed microscopically within 6 days. All images were acquired on a Zeiss LSM880 (Carl Zeiss AG, Oberkochen, Germany) in tile scan mode at a resolution of 2048×2048 px. For display, pictures were background subtracted and contrast was adjusted using ImageJ 1.52i.

RESULTS

Limbostomy: Design and Technical Data

In order to establish longitudinal intravital imaging of regeneration processes in long bones, we adapted the previously published LIMB microendoscopic system (31), based on an established, standardized fixator plate for osteotomies in mice (32). Simultaneously, we aimed to increase the FOV, to allow more flexibility regarding imaging depth, and maximize versatility by using only one multipurpose implant for both, osteotomy and imaging. A comparison of the FOV from the original LIMB system, the Limbostomy raw data, and the corrected images is illustrated in Supporting Information Figure 1 and Table S1. In order to combine an osteotomy model with LIMB, the osteotomy must be performed before the lens is inserted into the tissue. This is required to avoid damaging the lens and ensure free movement of the saw through the entire bone cortex. To achieve this, we chose a modular approach, in which the lens tubing is separated from the fixator plate and can be screwed into the plate using a thread on the lower end of the metal tubing (Fig. 1A). The thread terminates at the fixator plate, and only the lens sticks into the tissue (Fig. 1A, right). In this way, the lens can be attached after the injury is made (see also Fig. 3G). As a result, we were able to increase the diameter of the custom-built GRIN lens to 600 μm and simultaneously reduce the diameter of the tubing-lens-system inside the bone tissue by 50 μm , as compared to the previously published LIMB system. This resulted in less space occupied by the implant within the bone (Fig. 1B). Finally, in order to allow the introduction of an osteotomy gap and simultaneously maintain a stable fixation of the bone fragments, the screw positions lateral to the lens position were located equidistant and their intervening distance was maximized (Fig. 1C). In order to guarantee stable fixation, a minimum distance of one screw

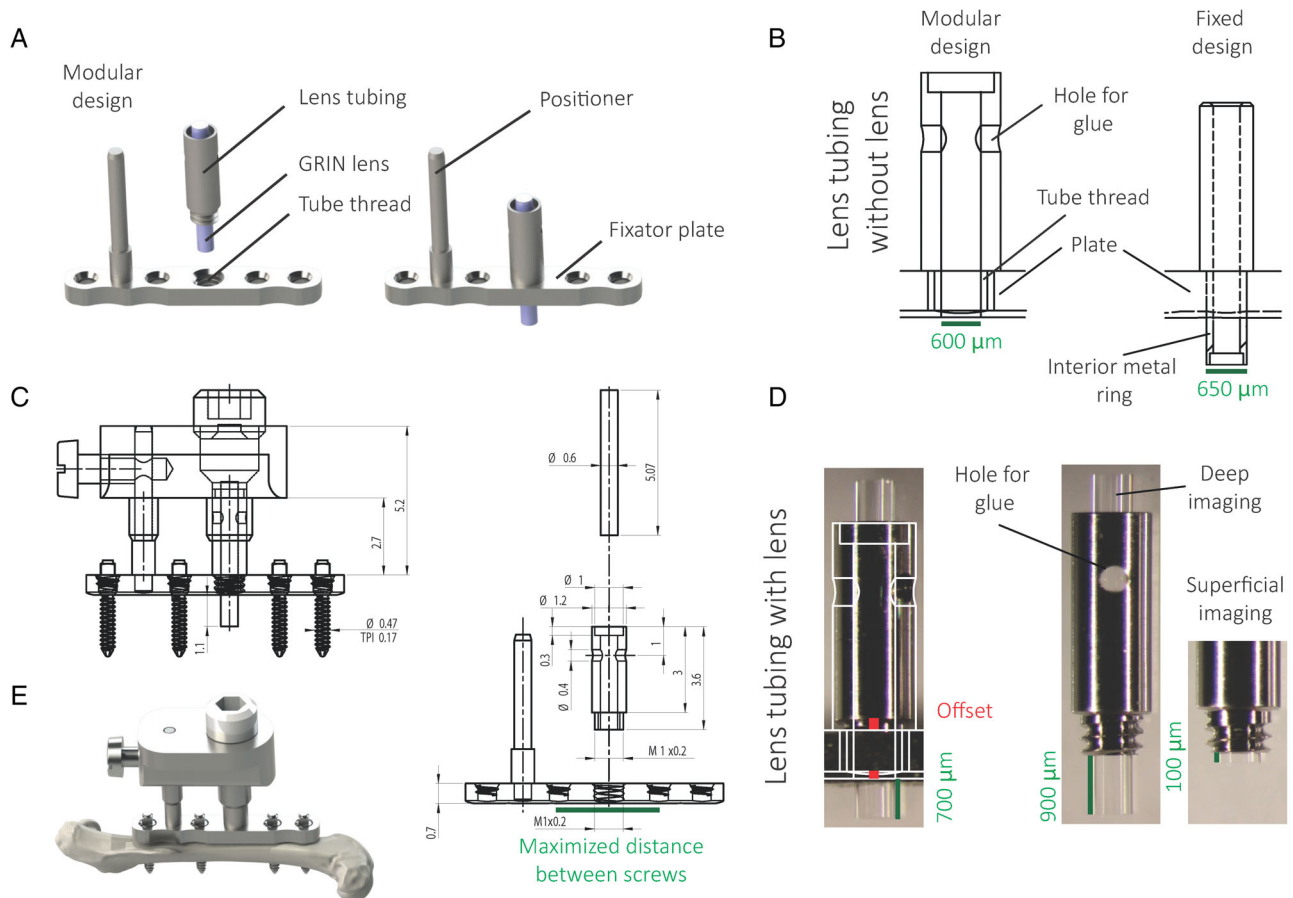


Figure 1. Limbostomy: a modular microendoscope design allows an increased imaging volume, varying depths, and secure fixation for an osteotomy. **(A)** An internal fixator plate with a rod for mounting the reference plate contains a thread which accepts the lens tubing. **(B)** In comparison to the fixed LIMB design, the interior metal ring is removed and allows the usage of a lens with a diameter of 600 μm . **(C)** The fully assembled Limbostomy design with mounted reference plate (left) and an exploded drawing of the fixator-lens design. Distances are in millimeters. The plate contains screw threads which are located in a maximal distance from the lens. **(D)** Pictures of glued tubing-lens modules. Offsets are due to production inaccuracy (upper offset, red) and the distance between the end of the tubing and the fixator (lower offset, red). In this example, the lens is glued protruding 900 μm (right), which results in 700 μm penetration depth (left). The lens can be glued protruding for superficial imaging. **(E)** Fully assembled, all modules are either glued or screwed together to secure the lens and prevent movement in the FOV.

diameter between two screws should be maintained (Romano Matthys, personal communication). The diameter of one screw is 0.47 mm (Fig. 1C). Consequently, as the distance between the screws amounts to 3.5 mm, the system allows for osteotomy gap sizes of up to 2 mm.

To enable visualization of bone regeneration processes, we aimed to access the center of the femoral long bone in an osteotomy. Based on the average femoral bone diameter of 1,415 μm , calculated from μCT data of 3-month-old mice (as published in Bucher et al.) (4), we glued the lens into the tubing at 900 μm protruding from the bottom of the fixation plate. This includes 700 μm bone and bone marrow as well as 200 μm offset between the plate and the bone surface, before the lens enters the bone. Offsets resulted from the contact-free design of the plate as well as from production inaccuracy, resulting in a variation of 100 μm (Fig. 1D).

The process of fixing the lens is performed manually, as shown in Supporting Information Movie S1. All these features in the Limbostomy system (Fig. 1E) allow the usage of flexible lens-tubing-systems with different penetration depths in the same, standardized fixator system, to achieve any depth up to 700 μm in the femoral bone, for osteotomy gap sizes of up to 2 mm.

Lens Characterization

Like in the LIMB system (31), a GRIN lens (Fig. 2A, Supporting Information Table S2) was used to optically access the bone tissue. In order to determine the relevant parameters for image correction in this two-photon fluorescence microendoscopy approach, we characterized its optical parameters and aberrations. These include chromatic aberration and spherical wave front aberrations.

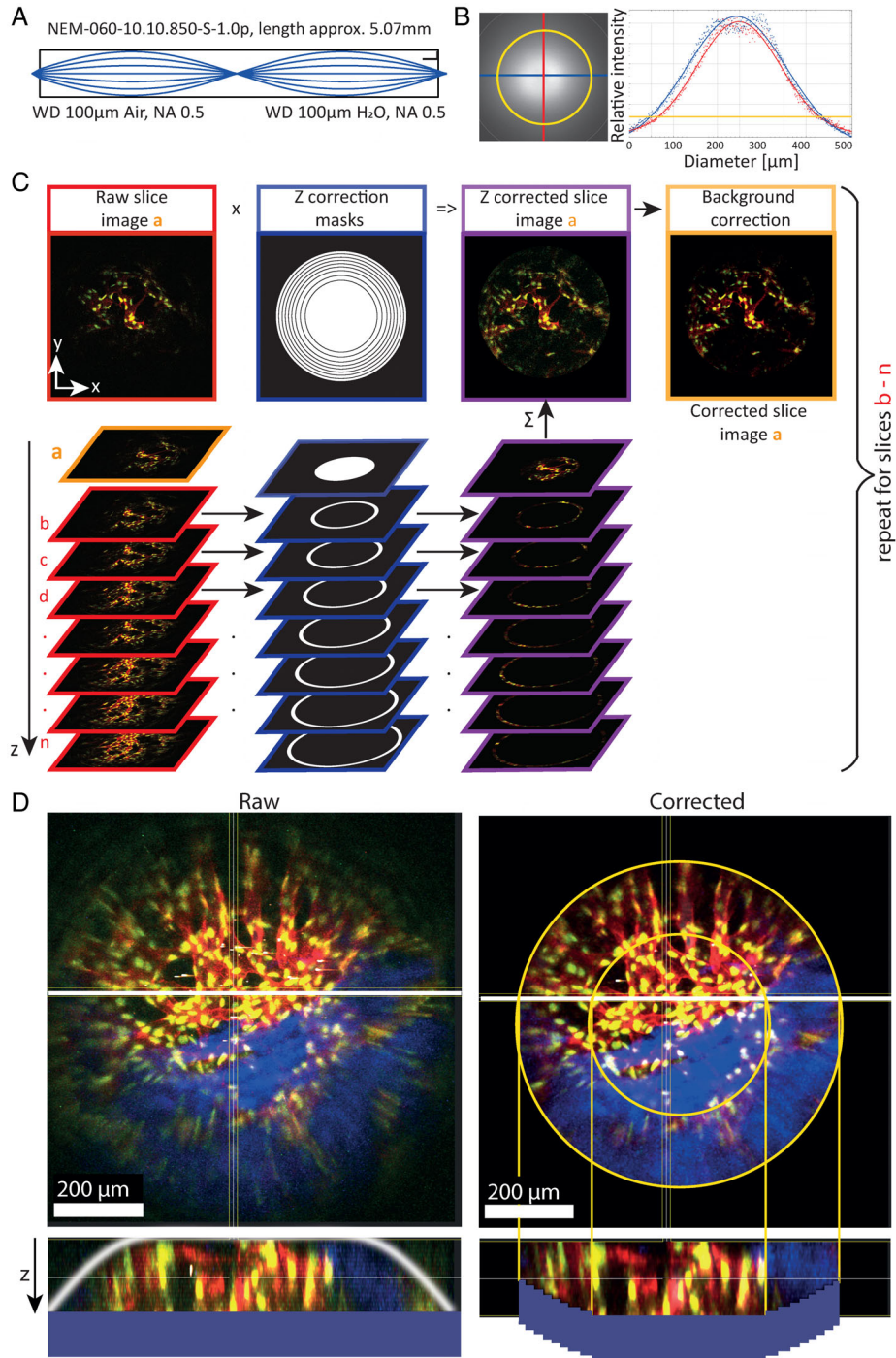


Figure 2. Lens specifications and image correction. **(A)** Designation of the used GRIN lens and technical drawing of the light path through the GRIN lens. **(B)** Field of view (yellow) with corresponding Gaussian fitted intensity distributions in x (blue) and y (red). **(C)** Flowchart visualization of the image correction algorithm. The raw slice image *a* (orange frame) gets z-corrected by shifting the displaced peripheral areas of lower slices up to their correct z position. This is done by cropping the concentric ring-shaped areas of lower slices (*b* to *n*) with binary masks (blue frame) and summing them up (purple frame). This is repeated for slices *b* to *n* as the new start points. Afterwards, a background correction is performed (yellow frame). **(D)** Comparison of the maximum intensity z-projections of raw image (left) and corresponding corrected image (right). The xz-section (of the white line) displays the image plane curvature in the raw and the up-shifted z-slices for the corrected image. Dark blue areas underneath symbolize deeper layers and illustrate how the image correction algorithm shifts deeper slices up to correct for displaced structures.

The FOV was determined based on the $1/e^2$ isoline of the maximum intensity from the lateral center of the illumination distribution through the GRIN lens (Supporting Information Fig. 2A), fitted by a Gaussian function (Fig. 2B). The field curvature and image distortions, which are mainly caused by chromatic and spherical aberrations, were quantified by imaging a reference grid with known dimensions and agarose gel containing fluorescent beads (200 nm diameter), respectively. An overview of all the determined optical parameters is depicted in the Supporting Information Table S2.

The chromatic aberration is defined as axial focal shift when the wavelength is changed. It was determined by sequentially imaging a rigid bead structure at different excitation wavelengths in the range between 800 and 1,030 nm, as we expect the chromatic aberration to scale linearly with the excitation wavelength (Supporting Information Methods Eq. 1, Fig. 2B). Since all analyses presented in this work were performed at the same excitation wavelength, no focal deviation was induced and therefore no correction of chromatic aberration was needed.

The third-order spherical aberration, which contributes significantly to the overall wave front aberration, resulted in a radial parabolic wave front and subsequent image plane deformation. This was quantified by imaging a defined reference grid, in which the radius of the sharpest grid structures, in relation to the focus depth, was measured. The data were fitted by a paraboloid model (Supporting Information Methods) using the least-squares fitting algorithm. Theoretically, in an ideal optical system with no wave front aberrations, the plane reference grid would appear as a sharp structure in one distinct focal plane. In our system, concentric ring-shaped areas appeared as sharp structures at various focal depths, indicating the deformation of peripheral areas of the image plane (Supporting Information Fig. 2C). This paraboloid distortion of the acquired images occurred along the optical axis.

Image Correction

In order to correct for the intrinsic confounding factors of the optical system, an image postprocessing algorithm of two main steps was designed. The first step sequentially corrects the slices of a raw stack (Fig. 2C, red frame) for image plane deformation introduced by the wave front aberrations in the axial dimension (Fig. 2C, purple frame). The second step corrects for system-related inhomogeneous illumination, sample-specific background signals and smoothes the signal in the images (Fig. 2C, yellow frame).

For z-corrections, binary polar masks were generated (Fig. 2C, blue frame) which depend on the z-step size of the raw image stack. The radius of each mask was calculated from the fitted equation (Supporting Information Methods Eq. 2), which best describes the image plane deformation in our experimental data (Supporting Information Fig. 2D). Afterwards, the masks are used to crop the corresponding concentric ring-shaped areas of lower slices in the z-stack, with a similar z-shift as the one caused by the third-order spherical aberration. The cropped image slices are merged at the

corrected z-position. This compensated the curvature of aberration-induced image plane deformation. The procedure was repeated iteratively with all z-slices as start points.

Image correction resulted in a visual improvement of the peripheral image areas through higher contrast and minimizing positional errors of structures in z (Fig. 2D). We validated the image correction algorithm by calculating and comparing the image plane curvature of raw and corrected images. We found that image quality was increased, and the image plane curvature was minimized (Fig. 2, Supporting Information Methods).

Surgery Procedure for Combined Imaging and Osteotomy

The femoral shaft of the right hind limb of a mouse was approached laterally and exposed under sterile conditions. Anesthesia via a respiratory mask was induced with 2.0% and maintained with 1.5% isoflurane. The mouse was positioned on a heating mat and the shaved and disinfected leg, covered by incision foil, was secured on a custom-made leg platform (Fig. 3A, Supporting Information Fig. 3). An incision of approximately 1.5 cm was made into the skin between the knee and hip joint, parallel to the femur (Fig. 3B, upper picture). The underlying muscles were dissected and retracted along the delimiting fascia (Fig. 3B, lower picture). The fixation plate was fixed onto the exposed bone and stabilized using forceps with a side lock (Fig. 3C, upper picture). A pilot hole was introduced at the distal screw thread position using a 0.31 mm drill bit (Fig. 3C, upper picture) and a 2 mm bicortical screw was inserted manually through the complete shaft and locked into the plate (Fig. 3C, lower picture). The process was repeated for the proximal screw position and the two remaining centered positions; so four screws were placed in total. In order to expose and access the full perimeter of the femur, forceps were placed under the bone (Fig. 3D,E, upper picture) and a Gigli wire saw of approximately 25 cm in length was passed through the gap (Fig. 3D). The two cutting positions were marked by placing small incisions with the saw. Cuts distal (Fig. 3E, lower picture) and proximal (Fig. 3F, upper picture) were made perpendicular to the bone and the bone section was removed (Fig. 3F, lower picture). Subsequently, the lens-tubing was positioned using a hand drill with enlarged drill chuck and screwed into the designated thread over the osteotomy gap (Fig. 3G). The wound was sewed with a surgical thread (Fig. 3H, upper picture). Finally, a reference plate was attached, fixed on the positioner, and closed using a plug screw to protect the lens (Fig. 3H, lower picture). The final result (Fig. 3I) shows the fixed reference plate outside the bone. We measured the gap size based on the distance between the screws and found that we reliably achieve a gap size of $\sim 816 \mu\text{m}$ (confidence interval (CI): 787–844 μm ; SD = 85 μm) (Fig. 3J). As shown previously, the wound heals without impacting the behavior of the mice (Reismann et al., Fig. 3K) (31). Using immunofluorescence histology, we observed normal regeneration and vessel formation at the site of injury indicated by high expression of Endomucin (Emcn) in areas of tissue damage and callus

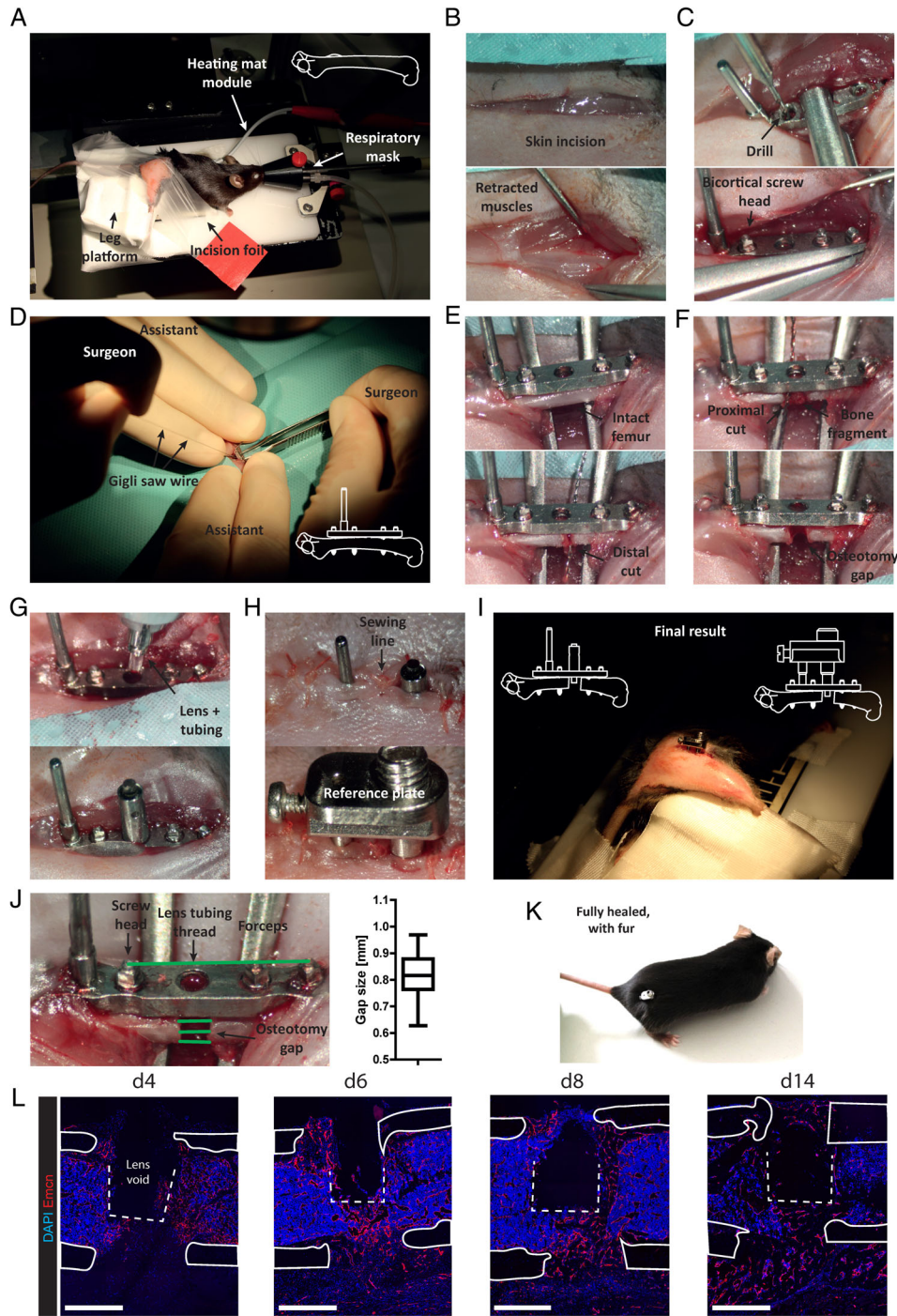


Figure 3. Limbostomy surgical procedure and healing outcome. (A) The mouse’s leg is shaved, and the mouse is fixed on a heating mat under isoflurane anesthesia. (B) An incision is made through the incision foil, skin and then muscles are retracted. (C) Guide holes are drilled and screws positioned. (D) Using a Gigli saw wire two cuts (E, F) are made and the bone fragment is removed. (G) The lens tubing is screwed into the fixator and (H) the skin closed before the reference plate is mounted onto the system. (I) The final result shows the reference plate outside of the body. (J) Osteotomy gap size was measured using the distance between screws as reference. Box-plot whiskers max–min (confidence interval, CI: 787–844 μm ; SD = 85 μm ; n = 37). (K) Fully healed, the mouse is not restricted in its movement and fur regrows. (L) Immunofluorescence histology of bone sections shows high expression of the vessel marker Endomucin (Emcn, red) in areas of tissue damage and callus formation over the course of regeneration. Nuclei are stained with DAPI and shown in blue. Images represent n \geq 4 for each time point. Scale bars = 500 μm .

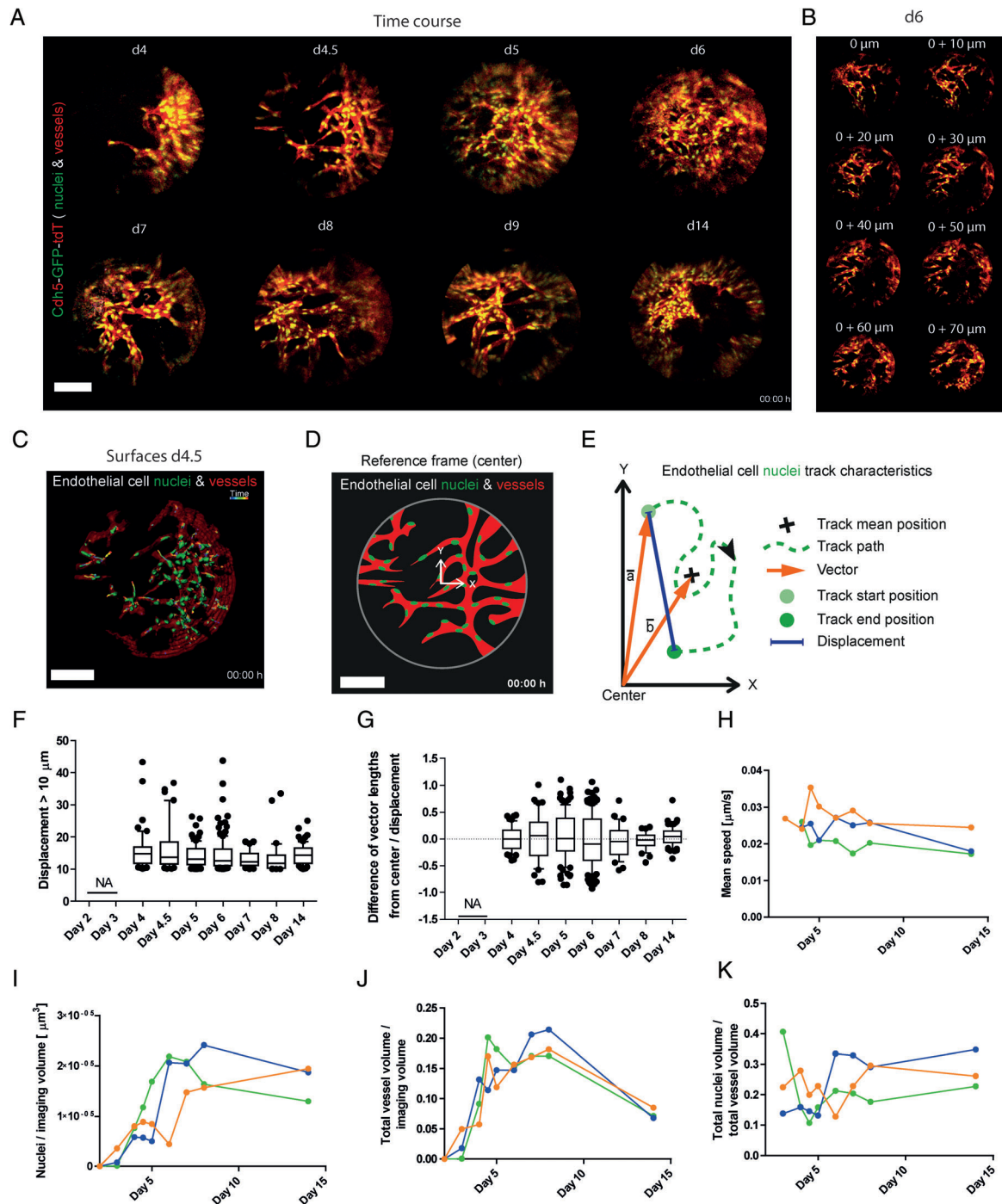


Figure 4. Vascularization after osteotomy is a highly dynamic process shown using Limbostomy. **(A)** Time course of vascularization over 2 weeks in an individual *Cdh5-GFP-tdT* mouse. Pictures are corrected maximum intensity projections of the FOV. The movies for Day 4 and Day 4.5 can be found in the Supporting Information Movie S4. **(B)** Projections of 10 μm thick slices of the z-stack resolve individual vessels. **(C)** Representative surface reconstructions of endothelial cell vessel volumes and nuclei as well as their tracks over time (rainbow colors). **(D)** Reference frame position in the FOV for direction of endothelial cell nuclei movement. **(E)** Object/endothelial cell nuclei track characteristics used for generating the difference of vector lengths from center ($|\vec{a}| - |\vec{b}|$). **(F)** Displacement and **(G)** normalized difference of vector lengths from center over time in one individual mouse (corresponding to the green curves in **H–K**). **(H)** Mean speed of nuclei, **(I)** nuclei count/imaging volume, **(J)** vessel volume based on tdT signal/imaging volume, and **(K)** the nuclei volume/vessel volume ratio for three individual mice. Scale bars = 100 μm .

formation shown to highly express PECAM-1 (CD31) (Fig. 3L) (45). Emcn expression was lower in contralateral bones, with only few Emcn^{hi} vessels alongside the endosteum (Supporting Information Fig. 4A). Of note, intraindividual bone regeneration progress showed variability of callus formation in front of the lens (Supporting Information Fig. 4B). All necessary utensils for the procedure are listed in the Supporting Information Table S3.

Longitudinal Imaging of Vessel Formation During Regeneration After Osteotomy

During healing, a close interplay of mesenchymal, vascular, and immune cells is required to initiate the regenerative process. Recently, we reported dynamic changes occurring in the vasculature during the tissue regeneration process after bone injury. We also reported vessel plasticity in homeostasis, when analyzed by longitudinal intravital microscopy, using intravenously injected Qtracker 655 Vascular Labels to highlight the vessel lumen (31). These particles are cleared from the blood by the kidney within 30 min. Additionally, a fraction of the label diffuses from the vessel lumen into the bone marrow tissue through the fenestrated sinusoidal endothelium specific to this tissue (Supporting Information Movie S2). In order to analyze the spatial changes of vasculature in the osteotomy model and draw conclusions about both vessel structure and proliferative behavior of the endothelial cells, we implanted the Limbostomy system into Cdh5-GFP-tdT reporter mice. These mice express a membrane-tagged tandem tomato fluorescent protein (tdT) and histone 2B linked enhanced GFP under a transgenic VE-cadherin (Cdh5) promoter. We repeatedly performed imaging in the osteotomy gap over the time course of regeneration, starting at Day 2, up to Day 14 after osteotomy. As shown in Figure 4 and consistent with our observations using immunofluorescence histology (50), vascularization of the fracture hematoma became detectable between Day 3 and Day 4 in the FOV. Vessels developed sprouts into the non-vascularized tissue (Fig. 4A) and rapidly expanded in the FOV. Within 24 h, the entire FOV was pervaded with endothelial cells (Fig. 4A). Using LIMB, we were able to capture a cell division event, which took 30 min from the prophase, in which chromosomal condensation was visible until telophase, when chromosomes decondensate (Supporting Information Movie S3). However, this was the only cell division event we observed. Endothelial cell sprouts were exclusively derived from the existing Cadherin5-expressing vessel network, and not de novo from scattered single cells. Activated tip cells with fine filopodia protruded into the nonvascularized tissue. They preceded the nucleus of the endothelial cell. The nucleus then moved into the tip and was subsequently followed by the cell body (Supporting Information Movie S4). The high density of sprouts made it challenging to discriminate the cell bodies of individual endothelial cells. As many cells showed filopodia, it was not always possible to identify activated tip cells or stalk cells unambiguously. Tip cells from different sprouts contacted each other, suggesting the formation of anastomoses (Supporting Information Movie S4, d4.5). The new vessel network in the FOV was dense by Day

5 and Day 6. Here, individual vessels were best visible in image sections rather than maximum intensity projections of stacks (Fig. 4B). The network rapidly reorganized from day to day until collagen deposition was visible via SHG, in line with the phase of soft callus formation on Day 6 (Supporting Information Fig. 4C). At 14 days postsurgery, the imaging depth is 80 μm due to collagen deposition and bone mineralization. Immunofluorescence histology observation shows that callus formation within the FOV was dependent on the individual regeneration progress (Supporting Information Fig. 4B,C).

The vessel network is a highly dynamic structure, characterized by motility of endothelial cell nuclei and the endothelial cell structures. We reconstructed three-dimensional surfaces for the nuclei and vasculature and tracked nuclei over time (Fig. 4C). In order to draw conclusions about the direction of movement, a reference frame was positioned in the center of the imaging volume (Fig. 4D) and endothelial cell nuclei tracks were recorded in this coordinate system (Fig. 4E). In order to account for image instability inherent to this type of intravital imaging, only nuclei with a displacement of $>10 \mu\text{m}$ were considered moving nuclei. Along the recorded time course, nuclei were motile (Fig. 4F) with no apparent preferred direction of movement (Fig. 4G) or speed (Fig. 4H) even at Day 14 postsurgery. The overall count of nuclei per imaging volume increased over time between Day 3 and Day 7 postsurgery and was stable until Day 14 (Fig. 4I). Simultaneously, total vessel volume increased until Day 8 and decreased until Day 14 (Fig. 4J). We measured the ratio of nuclei volume/vessel volume in order to determine patterns of vessel density, which—somehow unexpected—remained stable over time (Fig. 4K).

DISCUSSION

In this work, we introduce a method for intravital microendoscopy in the bone suitable for established bone regeneration models, as well as for the analysis of the marrow niches in long bones. The new design has a postprocessing FOV of 402 μm in diameter with a flexible z volume of up to 100 μm imaging depth inside the tissue. Although this system is not suitable for tile scans, imaging time series are acquired at a resolution comparable with other intravital bone imaging approaches (20,46). Imaging depth is a challenge in intravital bone and bone marrow two-photon imaging approaches, because it is limited to about 150 μm below the bone surface (34). This is why in most studies, the easily accessible calvarial bone for bone imaging is used (3,14,16,18,20,21,23–25,34,46,47). Ramasamy et al. circumvent this problem by imaging the small, metatarsal bones (26). In another approach, the cortical bone of the tibia was milled down to a small diameter in order to increase imaging depth of the actual marrow tissue (15,17,19). As this method removes the periosteum, it creates an acute injury and inevitably initiates an immune reaction, in addition to likely impacting on blood supply via transcortical vessels (48). Therefore, it is not suitable for longitudinal studies. In order to avoid immune responses and infection, Kim et al. repeatedly close, apply antibiotic ointment, and open the wound in order to perform

longitudinal imaging (49). Using the Limbostomy system or the LIMB system, which both share the same internal fixator plate and screws, imaging can be performed for several months in one individual without losing stability of fixation or image quality (29,31). Although Limbostomy was only tested for a period of several days in this study, and considering the usage of the same internal fixator plate, we expect that Limbostomy and LIMB are equally stable over time.

Here, we show that, after the lens has been placed, depending on its position in the tubing, practically any depth between periosteum and bone marrow center at about 700 μm can be reached and imaged with an extra imaging depth of consistently 100 μm , without further invasive manipulation of the mouse during regeneration. Over the course of regeneration, the maximum imaging depth decreases, most likely dependent on the varying degree of deposition of collagen-containing extra-cellular matrix at different stages. As shown in the Supporting Information Figure 3C, the system allows visualization of vasculature in 80 μm of depth at 14 days postsurgery. It is embedded in collagen-rich structures which produce SHG signals upon two-photon excitation, indicating the formation of a hard callus. This opens up the opportunity to analyze cellular dynamics during the remodeling phase directly at the respective site in the tissue, and will enable insights into the cellular and extracellular dynamics of tissue organization during these late phases of bone regeneration. The flexibility of the system with regard to insertion depth of the lens will allow us to adjust the position of the FOV according to the biological question. As known from histology studies, the callus resolves and becomes replaced by hematopoietic marrow tissue at later phases of regeneration in deeper regions of the bone (50). Limbostomy will us to analyze this important and fascinating process at cellular resolution. Any other method is limited to the 2PM imaging depth starting periostally approximately 150 μm below the bone surface (34), due to the highscattering properties of the bone, which are unique among mammalian tissues.

Compared to our initial LIMB system, Limbostomy has an increased FOV, flexible imaging depth, and occupies less space in the tissue due to a decreased diameter of the lens-tubing. This reduction of spatial limitations is combined with an increase in functionality and reproducibility. The Limbostomy system is the only system, which allows observation of bone regeneration in the long bones by stable fixation. The rigidity of the bone fixation influences the mechanical stability. It will be interesting to compare the impact of various degrees of fixation rigidity with respect to the process of regeneration longitudinally, at a cellular level. Here, we describe for the first time dynamic processes of endochondral bone regeneration in an osteotomy model, longitudinally, *in vivo*. The flexibility of the modular Limbostomy method can be considered an approach for multiple applications, such as the observation of cellular niches under homeostatic conditions (31), regeneration of drill holes injuries using a very short lens, regeneration of osteotomies of up to 2 mm size, over time in one individual, at cellular and subcellular resolution. It is theoretically possible to image endosteal areas

diametrically opposite the lens insertion site, by inserting the lens even deeper than the 700 μm mentioned above. Complementary, the drill hole injury at the insertion site can be investigated by positioning the lens to a penetration depth of 0.

Importantly, bone regeneration is a process with rapid phases such as the onset of vascularization or the distribution of inflammatory cells (50). Vascularization in the fracture gap is completed within 24 h after onset. However, the onset itself is observed to occur at Day 3 or Day 4 and therefore varies up to 24 h in our measurements. Comparing time points in early regeneration of samples from multiple individuals does not resolve these differences and subsequently results in high interindividual variations, which have also been reported by others (44). Using Limbostomy, it is now possible to describe the longitudinal process of regeneration of one individual in detail. This will allow a comparison between individuals in order to determine which stage of regeneration is delayed or accelerated. The increase of data gained from individuals is a good example of how intravital microscopy can also contribute to the Reduce, Refine, & Replace (3R) principle, which aims to improve design of experiments involving animals. Here, the animals undergo one surgery from which they recover quickly. From there, mounting and imaging includes few steps, with minimal impact on the animal or on physiological and inflammatory processes.

For this new microendoscope design, the FOV could be increased by a factor of 1.78 in comparison to the old GRIN lens approach (31) (Supporting Information Table S1) without decreasing resolution or sensitivity. Both the theoretical ($\Delta xy_{\text{theo}} = 0.75 \mu\text{m}$, $\Delta z_{\text{theo}} = 6.38 \mu\text{m}$) and experimental values ($\Delta xy_{\text{exp}} = 0.99 \pm 0.13 \mu\text{m}$, $\Delta z_{\text{exp}} = 6.44 \pm 1.29 \mu\text{m}$) we determined for the resolution showed minimal deviations. Importantly, not only the calculated resolution values, but also the fact that events such as the phases of mitosis could be observed in GFP-labeled nuclei, demonstrated the ability of the optical system to reach subcellular resolution in the context of the bone marrow environment.

GRIN lens technology in combination with a suitable objective in our system lead to optical errors like chromatic and wave-front aberrations. This was corrected using a post-processing algorithm which minimizes the axial image deformation and filters out noise and background signals.

The correction algorithm used here is adequate for the purpose of the performed image analysis, such as the investigation of the volume of nuclei, vessels, and directionality. An improvement of the image quality after image correction was achieved as demonstrated by experimental validation, which showed a decrease of the image plane curvature after correction (Supporting Information Fig. 5A,B), as well as the feature extraction of biological structures, which yielded more reliable and accurate results for the corrected images. In this way, subcellular resolution was achieved even in areas at the edge of the FOV.

Even though an xy-correction was not necessary in our case (Supporting Information Methods, Fig. 5C), it might become necessary when performing imaging at various

wavelengths, simultaneously or sequentially, since the third order spherical aberration is strongly dependent on the excitation wavelength. This holds true also for a correction of the chromatic aberration.

Using Limbostomy, we are for the first time able to observe the *de novo* formation of the vasculature after osteotomy, over extended time periods, in one and the same animal. Our method reveals that two phases of vascularization exist. The initial vascularization of the hematoma happens around 3–4 days after osteotomy, and by Day 4–5 the whole FOV is entirely pervaded with vessels. The second phase comprises remodeling of the vessel network, which occurs afterward, evident by the change in vessel volume between Day 8 and Day 14. This is in line with previous descriptions (2,51). The first wave of vascularization is rapid, since within 24 h the FOV is pervaded. Interestingly, this is the same time window as described in the much bigger bones of sheep (52). We have shown previously that dynamic changes occur in the vasculature during tissue regeneration, and high vessel plasticity was observed during homeostasis (31). Here, remodeling of the vasculature was observed over the entire process of regeneration, showing that vessel plasticity is also present during regeneration.

Sprouts show activated cells with filopodia, which are visible not only at the tip. The sprouts develop from the existing vessel network and migration into the non-vascularized areas is evident by movement of the nuclei of the stalk. In sprouting during vascularization of the neonatal retina, proliferation occurs in the stalk cells (53). Here, discrimination of tip, stalk, and network, which is a model used for vascularization of the retina (53) was challenging due to vessel density, ambiguous location of sprouts, as well as numerous filopodia at not only tip cells. Proliferation of endothelial cells during regeneration of the osteotomy was not observed, raising the question where those cells derive from. Proliferation of endothelial cells appears to be a rare event in bone tissue regeneration, as shown previously in histological Ki67 analysis after bone injury due to implantation of LIMB (31). In the retina, tip cells do not proliferate, but stalk cells do. It might be possible that proliferation occurs outside the FOV and the endothelial cells migrate into the injury. Another possibility is that the cell division events are so rare that we simply missed them. Here, extensive imaging times could be considered. Not only proliferation, but a complete characterization of the organization of endothelial cells during vascularization and reorganization in the bone regeneration process is of interest. Vascularization is essential for bone regeneration and Limbostomy will shed light on the cellular and subcellular mechanisms in this process. It was previously not possible to analyze tissue dynamics such as directional cell movement, object velocity, cell–cell interactions, anastomosis, sprouting, and collagen deposition during tissue regeneration in the long bones, because those types of analyses were limited to the calvarium.

In order to characterize metabolic conditions in the tissue on a cellular level, related to its perfusion, and analyze their impact on bone regeneration (6), the combination of

Limbostomy with fluorescence lifetime imaging (FLIM) holds great potential. FLIM allows the marker-free investigation of the NAD(P)H-related metabolism of cells (54). To overcome the limitation of decreased imaging depth in mineralized tissue, three-photon microscopy could be an interesting technique that may also be used in combination with Limbostomy. Combining Limbostomy with our recently developed technology for multiplexed intravital microscopy (55) will enable us to come closer to analyzing the complex dynamics of the regeneration process, as it will help to account for the known heterogeneity of bone marrow stromal cells (56,57).

The method of Limbostomy is suitable for applications in health and disease including the proliferation of stem and progenitor cells in their niches during hematopoiesis, mesenchymal cell–cell interactions, endothelial cell functions, or mobilization of cells during infections. It will enable longitudinal monitoring in the context of tumor formation and therapy, and will deliver a better understanding of immunological memory and long-lived cells *in vivo*. Furthermore, the wide range of applications for this method will contribute to standardization of intravital bone marrow imaging experiments and thereby increase comparability among those.

ACKNOWLEDGMENTS

We thank Christian Bucher for providing the measurements of bone thickness based on μ CT data. This study was funded by the Deutsche Forschungsgemeinschaft, Forschergruppe FOR2165 “Regeneration in Aged” (DFG grant 5354/6-2 to AEH), DFG TRR130, TP C01 to AEH and RAN and HA5354/8-1 to AEH. Parts of this work were supported by an “Adding 3R value” grant from the Charité - Universitätsmedizin Berlin. JS is a member of the Berlin-Brandenburg School for Regenerative Therapies (BSRT). AFF is a member of the Dahlem Research School (DRS). AFF is supported by a PhD scholarship of the Beuth Hochschule für Technik Berlin.

CONFLICT OF INTEREST

RM and RN (RISystem AG, Landquart, Switzerland) declare competing financial interests. The implant for longitudinal imaging will be commercialized by RISystem AG, Landquart, Switzerland. The remaining authors declare no competing financial interests.

AUTHOR CONTRIBUTIONS

AEH, RAN, JS, RM, RN, GND, and DR developed the modular implant approach. JS, AFF, MK, WL, MT, RG, and AR performed experiments. JS, AFF, AR, WL, and MT analyzed the data. RHA and MGB provided Cdh5-tdTHistone2B-GFP mice. AEH, RAN, JS, and AFF interpreted the results and wrote the manuscript. RM, RN, MK, AR, and GND reviewed the manuscript.

LITERATURE CITED

1. Einhorn TA, Gerstenfeld LC. Fracture healing: Mechanisms and interventions. *Nat Rev Rheumatol* 2014;11:45–54.

2. Schmidt-Bleek K, Petersen A, Dienelt A, Schwarz C, Duda GN. Initiation and early control of tissue regeneration - bone healing as a model system for tissue regeneration. *Expert Opin Biol Ther* 2014;14:247-259.
3. Fujisaki J, Wu J, Carlson AL, Silberstein L, Putheti P, Larocca R, Gao W, Saito TI, Celso CL, Tsuyuzaki H, et al. In vivo imaging of Treg cells providing immune privilege to the haematopoietic stem-cell niche. *Nature* 2011;474:216-219.
4. Bucher CH, Schlundt C, Wulsten D, Sass FA, Wendler S, Ellinghaus A, Thiele T, Seemann R, Willie BM, Volk HD, et al. Experience in the adaptive immunity impacts bone homeostasis, remodeling, and healing. *Front Immunol* 2019;10:797.
5. Reinke S, Geissler S, Taylor WR, Schmidt-Bleek K, Juelke K, Schwachmeyer V, Dahne M, Hartwig T, Akyuz L, Meisel C, et al. Terminally differentiated CD8 + T cells negatively affect bone regeneration in humans. *Sci Transl Med* 2013;5:177ra36.
6. Ambrosi TH, Scialdone A, Graja A, Gohlke S, Jank AM, Bocian C, Woelk L, Fan H, Logan DW, Schürmann A, et al. Adipocyte accumulation in the bone marrow during obesity and aging impairs stem cell-based hematopoietic and bone regeneration. *Cell Stem Cell* 2017;20:771-784.
7. Dimitriou R, Tsiroidis E, Giannoudis PV. Current concepts of molecular aspects of bone healing. *Injury* 2005;36(12):1392-1404.
8. Alexander KA, Chang MK, Maylin ER, Kohler T, Müller R, Wu AC, Van Rooijen N, Sweet MJ, Hume DA, Raggatt LJ, et al. Osteal macrophages promote in vivo intramembranous bone healing in a mouse tibial injury model. *J Bone Miner Res* 2012;188:1201-1205.
9. Schlundt C, El Khassawna T, Serra A, Dienelt A, Wendler S, Schell H, van Rooijen N, Radbruch A, Lucius R, Hartmann S, et al. Macrophages in bone fracture healing: Their essential role in endochondral ossification. *Bone* 2015;106:78-89.
10. Wu AC, Raggatt LJ, Alexander KA, Pettit AR. Unraveling macrophage contributions to bone repair. *Bonekey Rep* 2013;2:1-7.
11. Ono T, Okamoto K, Nakashima T, Nitta T, Hori S, Iwakura Y, Takayanagi H. IL-17-producing $\gamma\delta$ T cells enhance bone regeneration. *Nat Commun* 2016;7:10928.
12. Niesner RA, Hauser AE. Recent advances in dynamic intravital multi-photon microscopy. *Cytometry Part A* 2011;79A:789-798.
13. Ding L, Saunders TL, Enikolopov G, Morrison SJ. Endothelial and perivascular cells maintain haematopoietic stem cells. *Nature* 2012;481:457-462.
14. Itkin T, Gur-Cohen S, Spencer JA, Schajnovitz A, Ramasamy SK, Kusumbe AP, Ledergor G, Jung Y, Milo I, Poulos MG, et al. Distinct bone marrow blood vessels differentially regulate haematopoiesis. *Nature* 2016;532:323-328.
15. Köhler A, Schmthorst V, Filippi MD, Ryan MA, Daria D, Gunzer M, Geiger H. Altered cellular dynamics and endosteal location of aged early hematopoietic progenitor cells revealed by time-lapse intravital imaging in long bones. *Blood* 2009;114:290-298.
16. Lassailly F, Foster K, Lopez-Onieva L, Currie E, Bonnet D. Multimodal imaging reveals structural and functional heterogeneity in different bone marrow compartments: Functional implications on hematopoietic stem cells. *Blood* 2013;122:1730-1740.
17. Köhler A, de Filippo K, Hasenberg M, van den Brandt C, Nye E, Hosking MP, Lane TE, Männ L, Ransohoff RM, Hauser AE, et al. G-CSF-mediated thrombopoietin release triggers neutrophil motility and mobilization from bone marrow via induction of Cxcr2 ligands. *Blood* 2011;117:4349-4357.
18. Mazo IB, von Andrian UH. Adhesion and homing of blood-borne cells in bone marrow microvessels. *J Leukoc Biol* 1999;66:25-32.
19. Zehentmeier S, Roth K, Cseresnyes Z, Sercan Ö, Horn K, Niesner RA, Chang HD, Radbruch A, Hauser AE. Static and dynamic components synergize to form a stable survival niche for bone marrow plasma cells. *Eur J Immunol* 2014;44:2306-2317.
20. Bixel MG, Kusumbe AP, Ramasamy SK, Sivaraj KK, Butz S, Vestweber D, Adams RH. Flow dynamics and HSPC homing in bone marrow microvessels. *Cell Rep* 2017;18:1804-1816.
21. V-H L, Lee S, Lee S, Wang T, Jang WH, Yoon Y, Kwon S, Kim H, Lee S-W, Kim KH. In vivo longitudinal visualization of bone marrow engraftment process in mouse calvaria using two-photon microscopy. *Sci Rep* 2017;7:1-10.
22. Lo Celso C, Wu JW, Lin CP. In vivo imaging of hematopoietic stem cells and their microenvironment. *J Biophotonics* 2009;631:619-631.
23. Scott MK, Akinduro O, Lo Celso C. In vivo 4-dimensional tracking of hematopoietic stem and progenitor cells in adult mouse calvarial bone marrow. *J Vis Exp* 2014; 91:1-7.
24. Sipkins DA, Wei X, Wu JW, Runnels JM, Côté D, Means TK, Luster AD, Scadden DT, Lin CP. In vivo imaging of specialized bone marrow endothelial microdomains for tumour engraftment. *Nature* 2005;435:969-973.
25. Wang L, Kamocka MM, Zollman A, Carlesso N. Combining intravital fluorescent microscopy (IVFM) with genetic models to study engraftment dynamics of hematopoietic cells to bone marrow niches. *J Vis Exp* 2017;121:54253.
26. Ramasamy SK, Kusumbe AP, Schiller M, Zeuschner D, Bixel MG, Milia C, Gamrekelashvili J, Limbourg A, Medvinsky A, Santoro MM, et al. Blood flow controls bone vascular function and osteogenesis. *Nat Commun* 2016;7:13601.
27. Xie Y, Yin T, Wiegand W, He XC, Miller D, Stark D, Perko K, Alexander R, Schwartz J, Grindley JC, et al. Detection of functional haematopoietic stem cell niche using real-time imaging. *Nature* 2009;457:97-101.
28. Chen Y, Maeda A, Bu J, DaCosta R. Femur window chamber model for in vivo cell tracking in the murine bone marrow. *J Vis Exp* 2016;113:1-9.
29. Dondossola E, Alexander S, Holzapfel BM, Filippini S, Starbuck MW, Hoffman RM, Navone N, de-Juan-Pardo EM, Logothetis CJ, Huttmacher DW, et al. Intravital microscopy of osteolytic progression and therapy response of cancer lesions in the bone. *Sci Transl Med* 2018;10:eaao5726.
30. Lindquist RL, Niesner RA, Hauser AE. In the right place, at the right time: Spatio-temporal conditions determining plasma cell survival and function. *Front Immunol* 2019;10:788.
31. Reismann D, Stefanowski J, Günther R, Rakhymzhan A, Matthys R, Nützi R, Zehentmeier S, Schmidt-Bleek K, Petkau G, Chang HD, et al. Longitudinal intravital imaging of the femoral bone marrow reveals plasticity within marrow vasculature. *Nat Commun* 2017;8:2153.
32. Matthys R, Perren SM. Internal fixator for use in the mouse. *Injury* 2009;40(Suppl 4):S103-S109.
33. Raggatt LJ, Alexander KA, Kaur S, Wu AC, MacDonald KPA, Pettit AR. Absence of B cells does not compromise intramembranous bone formation during healing in a tibial injury model. *Am J Pathol* 2013;182:1501-1508.
34. Lo Celso C, Fleming HE, Wu JW, Zhao CX, Míake-Lye S, Fujisaki J, Côté D, Rowe DW, Lin CP, Scadden DT. Live-animal tracking of individual hematopoietic stem/progenitor cells in their niche. *Nature* 2009;457:92-96.
35. Pinho S, Frenette PS. Haematopoietic stem cell activity and interactions with the niche. *Nat Rev Mol Cell Biol* 2019;20:303-320.
36. van den Bos T, Speijer D, Bank RA, Brömme D, Everts V. Differences in matrix composition between calvaria and long bone in mice suggest differences in biomechanical properties and resorption. Special emphasis on collagen. *Bone* 2008;43: 459-468.
37. Huiskes R, Rulmerman R, Van Lenthe GH, Janssen JD. Effects of mechanical forces on maintenance and adaptation of form in trabecular bone. *Nature* 2000;405:704-706.
38. Umemura Y, Nagasawa S, Honda A, Singh R. High-impact exercise frequency per week or day for osteogenic response in rats. *J Bone Miner Metab* 2008;26: 456-460.
39. Lim J, Lee J, Yun HS, Shin HI, Park EK. Comparison of bone regeneration rate in flat and long bone defects: Calvarial and tibial bone. *Tissue Eng Regen Med* 2013; 10:336-340.
40. Meng Q, Liang Y, Sarsfield S, Jiang W-c, Lu R, Dudman JT, Aponte Y, Ji N. High-throughput synapse-resolving two-photon fluorescence microendoscopy for deep-brain volumetric imaging in vivo. *Elife* 2019;8:1-24.
41. Jeong HW, Hernández-Rodríguez B, Kim JM, Kim KP, Enriquez-Gasca R, Yoon J, Adams S, Schöler HR, Vaquerizas JM, Adams RH. Transcriptional regulation of endothelial cell behavior during sprouting angiogenesis. *Nat Commun* 2017;8:726.
42. Lang A, Schulz A, Ellinghaus A, Schmidt-Bleek K. Osteotomy models - The current status on pain scoring and management in small rodents. *Lab Anim* 2016;50: 433-441.
43. Legland D, Arganda-Carreras I, Andrey P. MorphoLibJ: Integrated library and plugins for mathematical morphology with ImageJ. *Bioinformatics* 2016;32:3532-3534.
44. Kawamoto T, Kawamoto K. Preparation of thin frozen sections from nonfixed and undecalcified hard tissues using Kawamoto's film method (2012). *Methods Mol Biol* 2014;1130:149-164.
45. Lang A, Kirchner M, Stefanowski J, Durst M, Weber MC, Pfeiffenberger M, Damerou A, Hauser AE, Hoff P, Duda GN, et al. Collagen I-based scaffolds negatively impact fracture healing in a mouse-osteotomy-model although used routinely in research and clinical application. *Acta Biomater* 2019;86:171-184.
46. Hawkins ED, Duarte D, Akinduro O, Khorsheed RA, Passaro D, Nowicka M, Straszekowski L, Scott MK, Rothery S, Ruivo N, et al. T-cell acute leukaemia exhibits dynamic interactions with bone marrow microenvironments. *Nature* 2016;538:518-522.
47. Lo Celso C, Lin CP, Scadden DT, Celso CL. In vivo imaging of transplanted hematopoietic stem and progenitor cells in mouse calvarium bone marrow. *Nat Protoc* 2011;6:1-14.
48. Grüneboom A, Hawwari I, Weidner D, Culemann S, Müller S, Henneberg S, Brenzel A, Merz S, Bornemann L, Zec K, et al. A network of trans-cortical capillaries as mainstay for blood circulation in long bones. *Nat Metab* 2019;1:236-250.
49. Kim S, Lin L, Brown GAJ, Hosaka K, Scott EW. Extended time-lapse in vivo imaging of tibia bone marrow to visualize dynamic hematopoietic stem cell engraftment. *Leukemia* 2016;31:1-11.
50. Stefanowski J, Lang A, Rauch A, Aulich L, Köhler M, Fiedler AF, Buttgerit F, Schmidt-Bleek K, Duda GN, Gaber T, et al. Spatial distribution of macrophages during callus formation and maturation reveals close crosstalk between macrophages and newly forming vessels. *Front Immunol* 2019;10:2588.
51. Schmidt-Bleek K, Schell H, Lienau J, Schulz N, Hoff P, Pfaff M, Schmidt G, Martin C, Perka C, Buttgerit F, et al. Initial immune reaction and angiogenesis in bone healing. *J Tissue Eng Regen Med* 2012;8:120-130.
52. Lienau J, Schmidt-Bleek K, Peters A, Haschke F, Duda GN, Perka C, Bail HJ, Schütze N, Jakob F, Schell H. Differential regulation of blood vessel formation between standard and delayed bone healing. *J Orthop Res* 2009;27: 1133-1140.
53. Gerhardt H, Golding M, Fruttiger M, Ruhrberg C, Lundkvist A, Abramsson A, Jeltsch M, Mitchell C, Alitalo K, Shima D, et al. VEGF guides angiogenic sprouting utilizing endothelial tip cell filopodia. *J Cell Biol* 2003;161:1163-1177.
54. Leben R, Köhler M, Radbruch H, Hauser AE, Niesner RA. Systematic enzyme mapping of cellular metabolism by phasor-analyzed label-free NAD (P) H fluorescence lifetime imaging. *Int J Mol Sci* 2019;20:5565.
55. Rakhymzhan A, Leben R, Zimmermann H, Günther R, Mex P, Reismann D, Ulbricht C, Acs A, Brandt AU, Lindquist RL, et al. Synergistic strategy for multi-color two-photon microscopy: Application to the analysis of germinal center reactions in vivo. *Sci Rep* 2017;7:7101.
56. Addo RK, Heinrich F, Heinz GA, Schulz D, Sercan-Alp Ö, Lehmann K, Tran CL, Bardua M, Matz M, Löhning M, et al. Single-cell transcriptomes of murine bone marrow stromal cells reveal niche-associated heterogeneity. *Eur J Immunol* 2019;49: 1372-1379.
57. Holzwarth K, Köhler R, Philippen L, Tokoyoda K, Ladyhina V, Wählby C, Niesner RA, Hauser AE. Multiplexed fluorescence microscopy reveals heterogeneity among stromal cells in mouse bone marrow sections. *Cytometry Part A* 2018;93A: 876-888.